MNRAS **000**, 1–12 (2015) Preprint 27 November 2018 Compiled using MNRAS LATEX style file v3.0

The SAMI Galaxy Survey: mass-kinematics scaling relations

Dilyar Barat[1,3]⋆ Francesco D'Eugenio[1,2], Matthew Colless[1,3], Luca Cortese[3,8], Barbara Catinella[3,8], Sree Oh[1,3], Brent Groves[1,3], Scott M. Croom[3,4], Julia Bryant[3,4,6], Sarah M. Sweet[3,13] Nicholas Scott[3,4], Jesse van de Sande[3,4], Sarah Brough[12], Joss Bland-Hawthorn[4], I-Ting Ho[10], Iraklis Konstantopoulos[11], Jon Lawrence[6], Nuria Lorente[6], Anne M. Medling[1,7]†, Matt S. Owers[5], Samuel Richards[9], Michael Goodwin[6],

[1] *Research School for Astronomy & Astrophysics Australian National University Canberra, ACT 2611, Australia*
[2] *Faculty of Sciences, Department of Physics and astronomy, Krijgslaan 281, S9, 9000 Gent*
[3] *ARC Centre of Excellence for All Sky Astrophysics in 3 Dimensions (ASTRO 3D)*
[4] *Sydney Institute for Astronomy, School of Physics, A28, The University of Sydney, NSW, 2006, Australia*
[5] *Department of Physics and Astronomy, Macquarie University, NSW 2109, Australia*
[6] *Australian Astronomical Observatory, 105 Delhi Rd, North Ryde, NSW 2113, Australia*
[7] *Ritter Astrophysical Research Center University of Toledo Toledo, OH 43606, USA*
[8] *International Centre for Radio Astronomy Research, University of Western Australia, 35 Stirling Highway, Crawley WA 6009, Australia*
[9] *SOFIA Science Center, USRA, NASA Ames Research Center, Building N232, M/S 232-12, P.O. Box 1, Moffett Field, CA 94035-0001, USA*
[10] *Max-Planck-Institut für Astronomie, Königstuhl 17, D-69117 Heidelberg,Germany*
[11] *Atlassian 341 George St Sydney, NSW 2000*
[12] *School of Physics, University of New South Wales, NSW 2052, Australia*
[13] *Centre for Astrophysics and Supercomputing, Swinburne University of Technology, PO Box 218, Hawthorn, VIC 3122, Australia*

Accepted XXX. Received YYY; in original form ZZZ

ABSTRACT

We use data from the Sydney-AAO Multi-object Integral-field spectroscopy (SAMI) Galaxy Survey to study the dynamical scaling relation between galaxy stellar mass M_* and the general kinematic parameter $S_K = \sqrt{KV_{rot}^2 + \sigma^2}$, that combines rotation velocity V_{rot} and velocity dispersion σ. We show that the $\log M_* - \log S_K$ relation: (1) is linear above the spectral resolution limit of the SAMI survey; (2) has smaller scatter than either the Tully-Fisher ($\log M_* - \log V_{rot}$) or the Faber-Jackson ($\log M_* - \log \sigma$) relation; (3) has scatter that is only weakly sensitive to the value of K; (4) has minimum scatter for K in the range 0.4 and 0.7; and (5) applies to both early-type and late-type galaxies. We compare S_K to the aperture second moment (the 'aperture velocity dispersion') measured from the integrated spectrum within a 3-arcsecond radius aperture ($\sigma_{3''}$). We find that while S_K and $\sigma_{3''}$ are in general tightly correlated, the $\log M_* - \log S_K$ relation has scatter less than $\log M_* - \log \sigma_{3''}$ relation.

Key words: keyword1 – keyword2 – keyword3

1 INTRODUCTION

Galaxy scaling relations correlate observable quantities of galaxies and capture trends among physical properties. These properties can include galaxy stellar mass (M_*), half-light radius (R_e), rotation velocity (V_{rot}), velocity dispersion (σ), luminosity (L), surface brightness (Σ) and other measurable quantities (McGaugh et al. 2000). For example, the Faber-Jackson relation (FJ; Faber & Jackson 1976) links σ to L, and the Kormendy relation (Kormendy 1977) links Σ to R_e.

Galaxy scaling relations are convenient in predicting physical galaxy properties because they do not require analytic modelling of a galaxy's internal dynamics. Using scaling relations to estimate quantities such as distance and mass is

⋆ E-mail: Dilyar.Barat@anu.edu.au
† Hubble Fellow

(1) Sample	(2) Selection criteria for each galaxy	(3) Number of galaxies gas/stellar	(4) All have both gas & stellar measurements?	(5) Used in Figure(s)
A	All of V_{rot}, σ, $S_{0.5}$ must have less than 5% error for each galaxy.	446/322	False	2
B	$S_{0.5}$ has error less than 5%.	1378/1783	False	1 3
C	V_{rot} for both gas and stellar measurements has error less than 5%.	258/258	True	4a
D	σ for both gas and stellar measurements has error less than 5%.	1038/1038	True	4b
E	$S_{0.5}$ for both gas and stellar measurements has error less than 5%.	987/987	True	4c
F	Both $S_{0.5}$ and $\sigma_{3''}$ have error less than 5%.	980/1250	False	5 6
G	Both V_{rot} and σ for both gas and stellar measurements have error less than 10%.	410/410(ETG) 232/232 (LTG) 737/737(All type)	True True True	7

Table 1. Sample selection criteria and description.

efficient when the sample size is too large to obtain detailed observations or to perform individual analyses.

Scaling relations such as the FJ and Kormendy relations have significant intrinsic scatter that impacts the accuracy of their predictive powers. Sample pruning and target selection are necessary to produce tight relations. For morphologically defined classes of galaxies, the Tully-Fisher (TF; Tully & Fisher 1977) relation provides a tight relation between L and V_{rot} for disk-dominated galaxies, and the Fundamental Plane relation (FP; Dressler et al. 1987; Djorgovski & Davis 1987) tightly relates R_e, σ and Σ for bulge-dominated galaxies.

Galaxy scaling relations are reflections of the physical mechanisms at work within galaxies. They enable us to gain deeper understanding of galaxy structure, formation and evolution. For example, Kassin et al. (2012) used V_{rot}/σ across redshift and found galaxies accrete baryons faster earlier in their life-cycles, and as galaxies evolve, their accretion rate and gas content decrease; Obreschkow & Glazebrook (2014) found the specific baryon angular momentum (j), stellar mass (M_*) and bulge fraction (β) of spiral galaxies are strongly correlated, and the $M_* - j - \beta$ scaling relation can produce and explain the FP (FJ) scaling relation; Lagos et al. (2017), using cosmological simulations, later confirmed the correlation between galaxy mass and specific angular momentum, and the evolution of the $M_* - j$ scaling relation in passive and active galaxies. Kinematic scaling relations are also useful in the study of galaxy dark matter content. For example, Desmond & Wechsler (2017) used the FP and predicted the existence of dark matter in the central regions of elliptical galaxies, and suggested the deviation of the FP from Virial prediction (also known as 'tilt' of the FP) can be explained by non-homology in galaxy structure and the variation in mass-to-light ratios; Ouellette et al. (2017) also found that the tilt of the FP correlates with the dark matter fraction of each galaxy.

The TF relation applies to disk-dominated galaxies while the FJ and FP relations apply to bulge-dominated galaxies. Incorporating galaxies of other morphologies into these scaling relations not only increases the scatter, but also changes the slopes and intercepts of the relations (e.g. Neistein et al. 1999; Iodice et al. 2003; Williams et al. 2010; Tonini et al. 2014), consequently reducing the accuracy and reliability of the quantities derived.

The scatter around the stellar mass versions of the FJ and TF relations can be reduced by replacing the rotation velocity or velocity dispersion with the S_K parameter introduced by Weiner et al. (2006):

$$S_K = \sqrt{KV_{rot}^2 + \sigma^2} \quad (1)$$

where K is a constant, commonly taken to be 0.5 (e.g., Weiner et al. 2006; Kassin et al. 2007; Covington et al. 2010; Kassin et al. 2012; Cortese et al. 2014; Simons et al. 2015; Straatman et al. 2017; Aquino-Ortíz et al. 2018). By combining V_{rot} and σ, S_K provides a common scaling relation for both early-type galaxies and late-type galaxies (Kassin et al. 2007). Furthermore, Cortese et al. (2014), using data from SAMI early data release, and Aquino-Ortíz et al. (2018), using data from the Calar Alto Legacy Integral Field Area survey (CALIFA; Sánchez et al. 2012), showed that S_K can bring together the gas and stellar kinematic measurements of galaxies of all morphologies onto a single dynamical scaling relation. Numerical simulation has shown S_K is minimally affected by the blurring effect due to seeing (Covington et al. 2010). Therefore, S_K is promising in the construction of a unified galaxy scaling relation that is robust with respect to morphologies and sub-optimal observing conditions. While

S_K has been a popular kinematic estimator and mass proxy, the following questions have not yet been fully answered:

(1) Is the scaling relation scatter sensitive to the value of K?

(2) Is the apparent non-linearity found by others (Cortese et al. 2014) in the $\log M_* - \log S_K$ relation physical?

(3) How does S_K compare to aperture velocity dispersion ($\sigma_{\rm ap}$) from single fibre surveys?

We use data from the Sydney-AAO-Multi-object IFS (Integral Field Spectroscopy) Galaxy Survey (hereafter SAMI survey; Croom et al. 2012; Bryant et al. 2015) to expand on the work of Cortese et al. (2014), and explore various aspects of the $\log M_* - \log S_K$ scaling relation. Our work is structured as follows. In Section 2, we describe the data reduction, kinematic measurements, and sample morphologies. In Section 3, we construct S_K from the gas and stellar measurements of our sample; compare S_K to aperture velocity dispersion ($\sigma_{3''}$) measurements; and explore the sensitivity of the scatter of the relation for different values of K. In Section 4, we compare our results to observations in the literature and discuss factors that influence the value of K. In Section 5 we summarise our conclusions. We assume throughout a ΛCDM cosmology with $\Omega_M = 0.3$, $\Omega_\lambda = 0.7$ and $H_0 = 70$ km/s/Mpc.

2 DATA & METHODS

The SAMI survey uses the AAOmega dual-beam spectrograph on the Anglo-Australian Telescope at Siding Spring Observatory (Sharp et al. 2006). SAMI obtains integral field spectra by using 13 fused-fibre hexabundles, each containing 61 fibres (Bland-Hawthorn et al. 2011; Bryant et al. 2014). The SAMI spectra cover the wavelength range 3750-5750 $\AA$ at a resolution of $R \sim 1808$, and 6300-7400 $\AA$ at a resolution of $R \sim 4304$ (Scott et al. 2018). These give dispersion resolutions $\sigma_{\rm res}$ of 70 km/s in the blue arm where we obtain the stellar kinematics, and 30 km/s in the red for gas kinematics.

The SAMI survey includes galaxies with redshifts $0.004 < z < 0.095$, r-band Petrosian magnitudes $r_{\rm pet} < 19.4$, and stellar masses $10^7 - 10^{12} M_\odot$. The stellar masses of SAMI galaxies are estimated as (Bryant et al. 2015):

$$\begin{aligned}\log(M_*/M_\odot) = &-0.4i + 0.4D - \log(1.0+z) \\ &+ (1.2117 - 0.5893z) \\ &+ (0.7106 - 0.1467z) \times (g-i) \end{aligned} \quad (2)$$

where M_* is the stellar mass in solar mass units, D is the distance modulus, i is rest frame i band apparent magnitude, and $g-i$ is the rest-frame colour of the galaxy, corrected for Milky-Way extinction (Bryant et al. 2015). More on the SAMI survey and instrument can be found in Croom et al. (2012).

2.1 Data Reduction & Sample

SAMI data reduction consists mainly of two stages, reducing raw data to row stacked spectra (RSS) using *2dfdr*[1], and data cube construction from the RSS using the *SAMI* *Python* package (Allen et al. 2014). The details of data reduction and data cubing processes can be found in Allen et al. (2015), Sharp et al. (2015), and Scott et al. (2018).

We used gas and stellar kinematic maps extracted from SAMI internal data release v0.10 data cubes. The systemic velocity and velocity dispersion maps are retrieved using the penalised Pixel Fitting method (pPXF; Cappellari & Emsellem 2004). pPXF extracts the stellar line-of-sight velocity distribution (LOVSD) in each spatial pixel (spaxel) from the

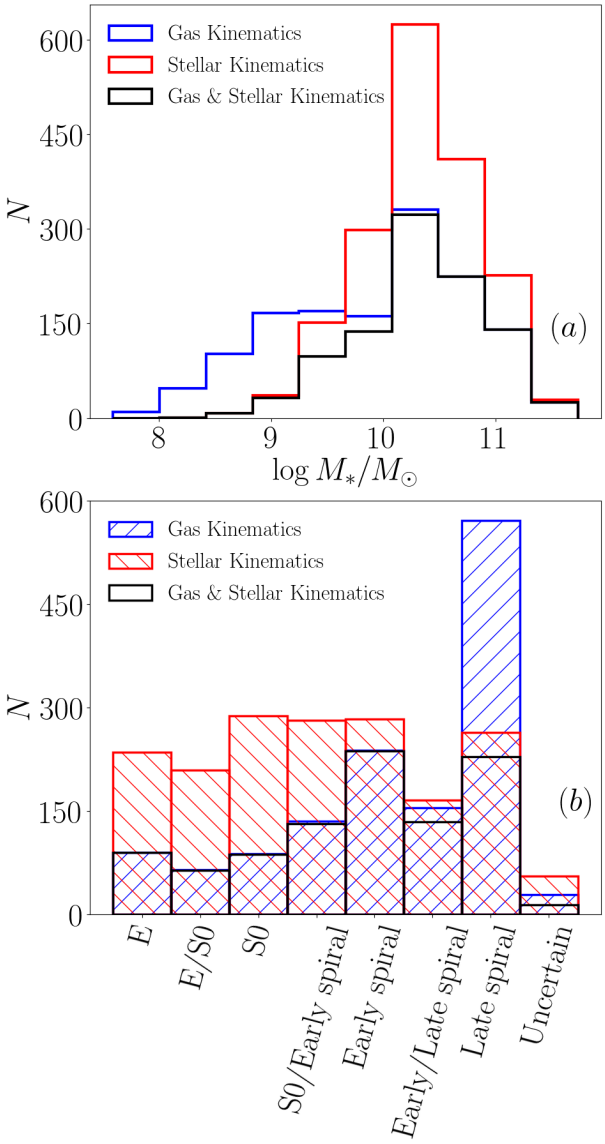

Figure 1. Panel (a) shows the mass distributions of sample B with various components available. Red represents galaxies with stellar kinematics; blue represents galaxies with gas kinematics; black represents galaxies with both gas and stellar kinematics. Panel (b) shows the visual morphology distribution of sample B. Red bars representing galaxies with stellar kinematics, blue bars represent galaxies with gas kinematics, and black bars represent galaxies with both gas and stellar kinematics.

[1] https://www.aao.gov.au/science/software/2dfdr

observed spaxel spectrum assuming a Gaussian form:

$$\mathcal{L}(v) = \frac{e^{-y^2/2}}{\sigma\sqrt{2\pi}} \quad (3)$$

where $y = (v - V)/\sigma$. The (V, σ) parameters of this model can be retrieved using a maximum likelihood optimisation. More details of the fitting routine can be found in van de Sande et al. (2017). As of August 2018, the stellar kinematic data sample includes 2720 galaxies, all of which have been fitted by the LZIFU (Ho et al. 2014) routine for $H\alpha$ emission line detection and measurement of the velocity and dispersion of the gas component.

Using the extracted SAMI stellar and gas kinematic maps, we select the spaxels as follows. First, spaxels are collected within an elliptical aperture with semi-major axis of one effective radius. For all SAMI galaxies, their semi-major axis, position angles and ellipticity are determined using Multi-Gaussian Expansion (MGE, Emsellem et al. 1994) fitting to r-band images from either the VLT Survey Telescope (VST) ATLAS (Shanks et al. 2015) survey or the Sloan Digital Sky Survey (SDSS). Contrary to Cortese et al. (2014) and Aquino-Ortíz et al. (2018), where spaxels are selected based on the absolute error of velocity and velocity dispersion, we do not perform spaxel-level quality cuts other than requiring galaxies to have more than 5 spaxels within the aperture. Instead, we perform an overall relative error cut on the kinematic parameter being investigated, only keeping galaxies with relative kinematic error less than 5%. Rotation velocity, velocity dispersion, S_K and associated error calculations are described in the next section.

Depending on the kinematic parameter to be studied and the selection criteria, our parent sample of 2720 galaxies is divided into 7 sample groups (group A-G). The selection criteria and sample group descriptions are listed in Table 1. For the $\log M_* - \log S_K$ scaling relation investigations we used sample B. Sample B includes gas-kinematics measurements for 1378 galaxies, stellar-kinematics measurements for 1783 galaxies, and 987 galaxies have both gas and stellar measurements. The median number of spaxels for galaxy in sample B is $\sim$ 70 spaxels. The stellar mass histogram in Figure 1a shows that sample B is relatively complete in the high-mass ($\geq 10^{10} M_\odot$) range, but with sufficient numbers of galaxies in the low-mass range to constrain a scaling relation.

2.2 Galaxy Kinematics

To calculate the rotation velocities of the gas and the stars, we use the velocity histogram technique, following Catinella et al. (2005) and Cortese et al. (2014). We calculate the velocity width W between the 90th and 10th percentile points of the histogram of spaxel velocities within one r-band effective radius (r_e) elliptical aperture. Then we perform redshift (z) and inclination (i) corrections using an inclination angle estimated from the r-band major-to-minor axes ratio which is obtained from the MGE fit to VST and SDSS images. The rotation velocity is calculated as:

$$V_{rot} = \frac{W}{2\,\sin i\,(1+z)}. \quad (4)$$

For all galaxies we assume an intrinsic axes ratio of 0.2 (Catinella et al. 2012). For galaxies where the axis ratio is greater than 0.98, we do not perform any inclination corrections to prevent over-correction on intrinsically oblate galaxies, and use only redshift-corrected rotation velocities. The histogram technique is simple to implement, and in the process of calculating the velocity width, the Hubble velocity and peculiar velocity of the system naturally cancel.

The effective velocity dispersion σ of a galaxy is measured as the luminosity-weighted mean of velocity dispersion measurements of each spaxel within an aperture radius of 1 effective radius.

$$\sigma \equiv \frac{\sum_i L_i \sigma_i}{\sum_i L_i} \quad (5)$$

We highlight that we do not perform any spaxel level quality cut here, other than having at least 5 spaxels. We then calculate $S_{0.5}$ as per Equation 1, with $K = 0.5$. To measure the uncertainty on the kinematic parameters, we use bootstrapping over all spaxels within the aperture for each galaxy, and use the standard deviations of V_{rot}, σ and $S_{0.5}$ as their uncertainties.

2.3 Galaxy Morphologies

Galaxy morphologies in SAMI galaxies vary from elliptical galaxies to late-type spiral and irregular galaxies. All SAMI galaxies are visually classified using the SDSS DR9 (Ahn et al. 2012) RGB images by 12 members of the SAMI team following the classification scheme adopted in Kelvin et al. (2014). Here we briefly summarise the classification scheme. First, judging by the presence/absence of a disk or spiral arms, the classifier determines whether a target is an early-type or late-type galaxy. Then in each class, classifiers visually determine if the galaxy contains a bulge (for late-type galaxies) or a disk (for early-type galaxies). Early-type galaxies with only a bulge, and without any disk component, are identified as elliptical galaxies (E); early-type galaxies that show both bulge and disk components are identified as S0 galaxies. Late-type galaxies all have spiral arms by classification definition; if there is a prominent bulge, then it is classified as early-spiral galaxy; and if there are only spiral arms without a central bulge, then it is classified as a late-spiral or irregular galaxy. Where the SDSS image does not show enough features, or a consensus ($> 67\%$) among classifiers is lacking, the galaxy is classified as Uncertain (Cortese et al. 2016). For sample B, where we have the most galaxies for the $\log M_* - \log S_{0.5}$ studies, their morphology distribution is shown in Figure 1b. There are relatively more early-type galaxies (elliptical to S0 galaxies) in the stellar sample, and more late-type galaxies (early- to late-type spirals) in the gas sample.

3 SAMI SCALING RELATIONS

3.1 $S_{0.5}$ reduces scatter

In this section we demonstrate the advantage of using the $S_{0.5}$ parameter in dynamical scaling relations in contrast to using V_{rot} and σ alone when using IFS data. In both Cortese et al. (2014) and Aquino-Ortíz et al. (2018), the $\log M_* - \log S_{0.5}$ scaling relation showed significant reduction in scatter when compared to the TF relation using V_{rot} and FJ relation using σ. For comparison, we perform the

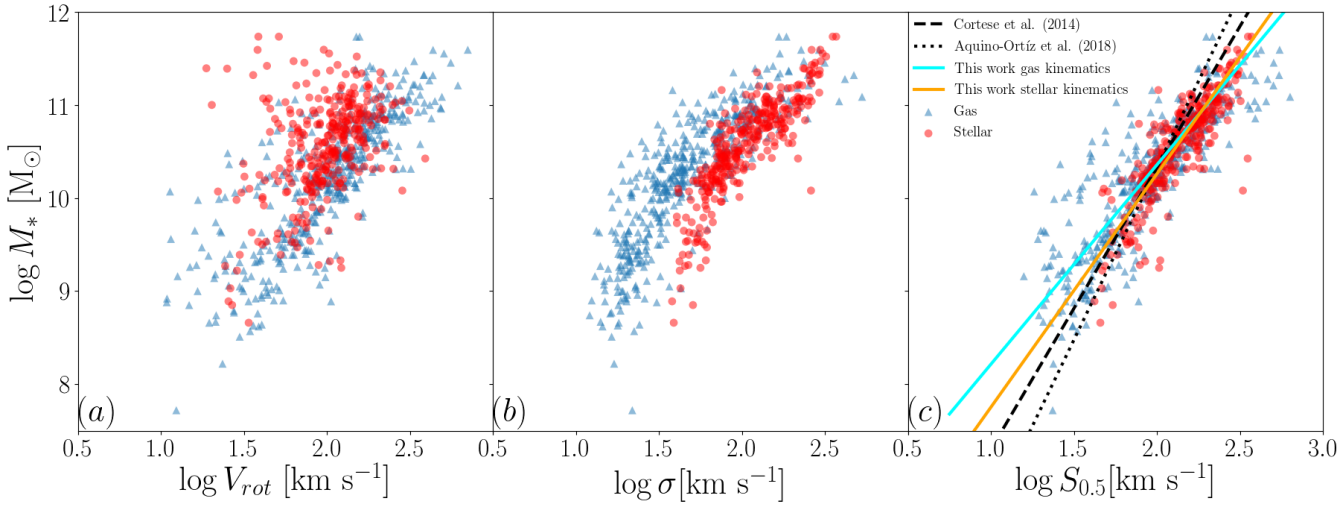

Figure 2. SAMI scaling relations from sample A: (a) Tully-Fisher, (b) Faber-Jackson, (c) generalised $S_{0.5}$ scaling relation. Red dots represent galaxies with stellar measurements, blue triangles represent gas measurements. In panel (c) the orange solid line is the best fit line to the stellar $\log M_* - \log S_{0.5}$ scaling relation, and the cyan solid line is the best fit line to the gas scaling relation. Relations found by Cortese et al. (2014) and Aquino-Ortíz et al. (2018) are included for comparison; they are represented by the black dashed line and black dotted line respectively.

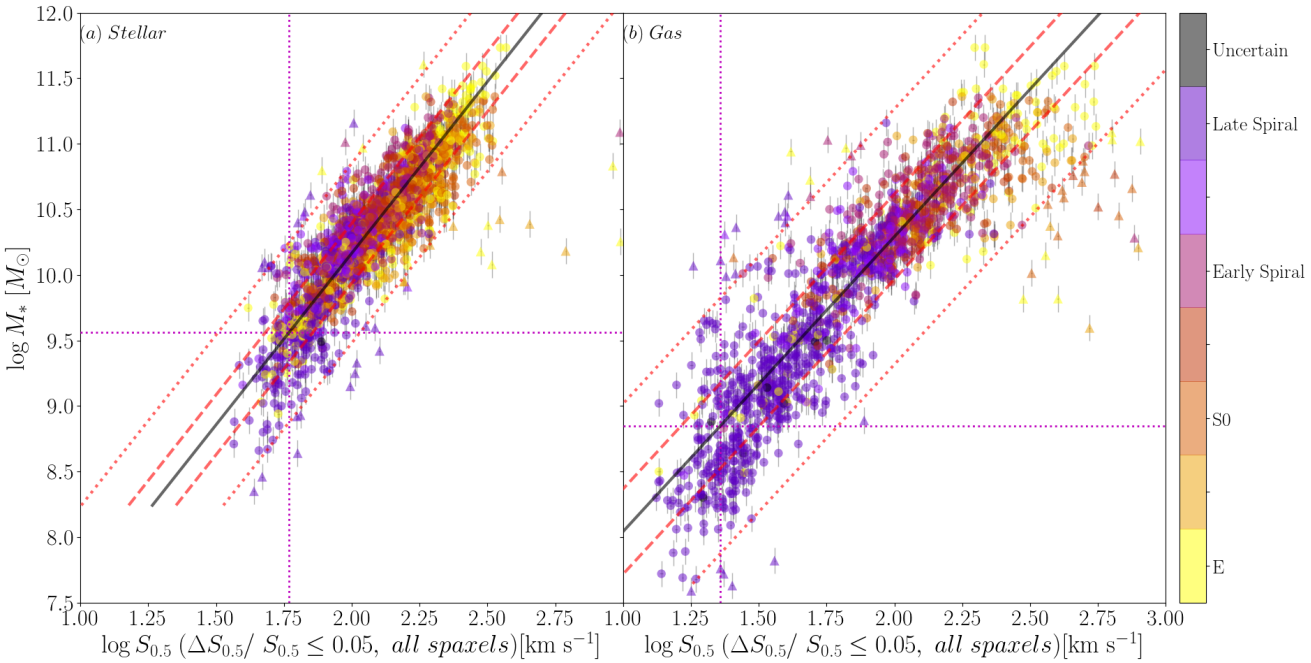

Figure 3. SAMI stellar and gas $S_{0.5}$ scaling relations from sample B. Black solid line shows the line of best fit, with fitting parameters shown in Table 2. Red dashed and dotted lines show 1 and 3 RMS distance from the line of best fit. Triangular points are galaxies >3 RMS away from the line of best fit, and are excluded from the fitting routine. The magenta vertical and horizontal dotted lines show the location where the distribution of points deviate from a linear relation, which we fit as the kinematic measurement limit. These limits occur at different $S_{0.5}$ values and different stellar masses for the stellar and gas samples. $S_{0.5,\mathrm{lim,stellar}} = 59$ km/s for the stellar sample, $S_{0.5,\mathrm{lim,gas}} = 23$ km/s for the gas sample. These $S_{0.5,\mathrm{lim}}$ values are just below the nominal instrumental dispersion, respectively, the blue-arm SAMI spectra (for the stellar sample) and the red-arm SAMI spectra (for the gas, i.e. $H\alpha$ sample). This suggests the cause of the bend observed here is more likely a measurement limitation.

Sample	Figure	Y	Slope (a)	Intercept (b)	$Y_{\rm lim}$ [km/s]	$M_{*,\rm lim}[M_\odot]$	Scatter ($\rm MAD_{orth}$)
B	3a	$S_{0.5,\rm stellar}$	0.38 ± 0.01	-1.88 ± 0.06	58.9 ± 1.0	$10^{9.61}$	0.050 ± 0.001
	3b	$S_{0.5,\rm gas}$	0.44 ± 0.01	-2.57 ± 0.07	22.7 ± 1.0	$10^{8.92}$	0.073 ± 0.002
F	6a	$S_{0.5,\rm stellar}$	0.36 ± 0.01	-1.59 ± 0.05	67.0 ± 1.2	$10^{9.49}$	0.049 ± 0.001
	6c	$S_{0.5,\rm gas}$	0.40 ± 0.01	-2.14 ± 0.06	22.4 ± 1.0	$10^{8.73}$	0.061 ± 0.002
F	6b	$\sigma_{\rm stellar}$	0.38 ± 0.01	-1.82 ± 0.06	67.6 ± 1.1	$10^{9.61}$	0.068 ± 0.002
	6d	$\sigma_{\rm gas}$	0.48 ± 0.01	-2.98 ± 0.14	26.4 ± 1.1	$10^{9.17}$	0.090 ± 0.004

Table 2. Scaling relation fitting results from *hyper-fit*. All scaling relations have the form as described in Equation 8.

same comparison between $S_{0.5}$, V_{rot} and σ using sample A (as described in Table 1). In sample A, for each of the gas and stellar kinematic measurements, all of $S_{0.5}$, V_{rot} and σ have less than 5% error for all galaxies. Figure 2 shows the correlation of stellar mass (M_*) with V_{rot}, σ, $S_{0.5}$ (i.e. the stellar mass TF, FJ, and combined $S_{0.5}$ scaling relations) as constructed from sample A data. For both the gas and stellar versions of these scaling relations, the $\log M_* - \log S_{0.5}$ relation consistently has less scatter than the TF and FJ relations. A caveat here is that our V_{rot} measurements for late-type spiral galaxies do not reach the peak of their rotation curves, hence they cannot accurately trace the potentials of galaxies, and therefore in our "TF" relation V_{rot} is not as good as an estimator of M_* as $S_{0.5}$

The fits from Cortese et al. (2014) and Aquino-Ortíz et al. (2018) (from orthogonal fitting of the combined gas & stellar mixture sample) are shown in Figure 2c by dashed line and dotted line respectively. There is a small difference between the slopes for our gas and stellar sample in orange and cyan respectively, and those found by Aquino-Ortíz et al. (2018) and Cortese et al. (2014), but given the differences in our sample selection, survey systematics, and fitting methods, it is hard to interpret the observed slope difference as a physical difference.

3.2 Linearity of the $S_{0.5}$ scaling relation

Cortese et al. (2014) constructed the gas FJ and $\log M_* - \log S_{0.5}$ scaling relations and observed the slope became steeper for low mass ($M_* < 10^{10} M_\odot$) galaxies. This change in slope is also present in our FJ relation in Figure 2b, and the $\log M_* - \log S_{0.5}$ relations in Figure 2c. Cortese et al. (2014) speculated that this change in slope could be the result of using stellar mass rather than baryonic mass. Due to lack of sufficient HI data for our sample, we are unable to measure the baryonic mass in a statistically significant sense, therefore we cannot exclude the possibility of reducing the bend in the scaling relations by using baryonic mass. However, in Figure 2b, the changes in slope occur at different σ values for gas and stellar components, $\log \sigma_{gas} \sim 1.5$ and $\log \sigma_{stellar} \sim 1.8$. These σ values are close to our instrument resolutions as stated in Section 2, $\sigma_{\rm res,gas} \sim 30$ km/s, $\sigma_{\rm res,stellar} \sim 70$ km/s. To locate the change in slope in our $\log M_* - \log S_{0.5}$ scaling relations more precisely, we investigate the scaling relations in detail with sample B in Figure 3, where galaxies are selected only based on $\Delta S_{0.5}/S_{0.5} \leq 0.05$.

3.2.1 *Straight line with a knee*

In order to test the linearity of the scaling relations, and find the point at which the slope of the relation changes, we hypothesise that there exists a $S_{0.5}$ measurement limit, likely due to combination of spectral signal-to-noise ratio and instrumental resolution, and a corresponding $M_{*,\rm lim}$ value. For all stellar mass measurements below this $M_{*,\rm lim}$ value, $S_{0.5}$ values will be normally distributed around a limiting value $S_{0.5,\rm lim}$. For stellar mass above the $M_{*,\rm lim}$ value, the scaling relation is assumed to be a linear relation described by:

$$\log S_{0.5} = a \log M_* + b \tag{6}$$

We then use this combination of a linear model with a constant limit cutoff in our maximum likelihood fitting routine, assuming $\log M_{*,i}$, $\log S_{0.5,i}$ for each galaxy have Gaussian uncertainties $\sigma_{\log M_{*,i}}$, $\sigma_{\log S_{0.5,i}}$. The total posterior logarithmic likelihood $\ln \mathcal{L}$ of $\log S_{0.5}$ for given $\log M_*$, a, b, $\sigma_{\log M_{*,i}}$, $\sigma_{\log S_{0.5,i}}$, $\log M_{*,\rm lim}$ becomes

$$\ln \mathcal{L} = \frac{1}{2} \sum_i \left[\ln \frac{a^2+1}{s^2_{\log S_{0.5,i}}} - \frac{(\log S_{0.5,i} - Y)^2}{s^2_{\log S_{0.5,i}}} \right] \tag{7}$$

where Y is a linear function above $M_{*,\rm lim}$, and a constant below $M_{*,\rm lim}$, i.e.:

$$Y = \begin{cases} a \log M_{*,i} + b, & M_* > M_{*,\rm lim} \\ a \log M_{*,\rm lim} + b, & M_* \leq M_{*,\rm lim} \end{cases} \tag{8}$$

In Equation 7, $s^2_{\log S_{0.5,i}} \equiv \sigma^2_{\log S_{0.5}} + \sigma^2_{M_{*,i}} a^2 + \sigma^2_{\log S_{0.5,i}}$. Here $\sigma_{\log S_{0.5}}$ is the intrinsic vertical scatter of the model and $\sigma_{\log S_{0.5,i}}$ is the measurement uncertainty in $S_{0.5}$ for data point i. By adjusting the fitting parameters a, b, $\sigma_{\log S_{0.5}}$, $\log M_{*,\rm lim}$ and sampling around the best fitting results using Markov chain Monte Carlo (MCMC; Foreman-Mackey et al. 2013), we can find the most likely fitting model to the data that maximises Equation 7 together will the parameter uncertainties. To ensure the model is robust against outliers, we repeat the fitting routine 5 times whilst rejecting points that are $> 3\sigma$ away. The fitting method is described in more detail as the 2 dimensional *hyper-fit* in Robotham & Obreschkow (2015).

3.2.2 *The bends in the scaling relations*

Following the fitting methods described in Section 3.2.1, we fit the linear model with a cutoff to our sample B galaxies, as shown in Figure 3. There are a few outliers in our stellar and gas scaling relations. In the stellar scaling relation, galaxies with high $S_{0.5}$ values ($\geq 10^{2.5}$ km/s) are visually found to

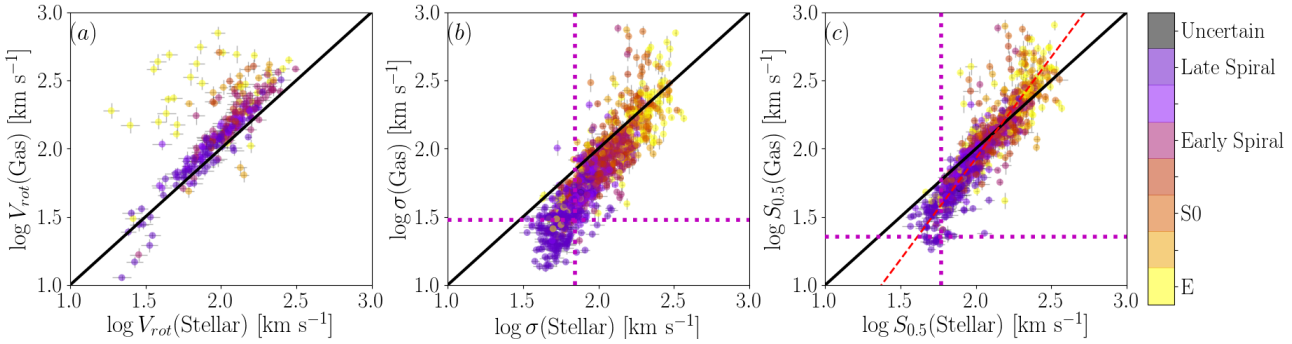

Figure 4. Comparison between SAMI sample C, D, E, gas and stellar measurements of (a) V_{rot}, (b) σ, and (c) $S_{0.5}$. Galaxies are colour coded by morphologies. We show 3 standard deviation error bar here to ensure error bars are visible. Black solid lines in each panel show the one-to-one relation. The red dashed line in panel (c) is the best fit line to the points. Horizontal and vertical magenta lines in panel (b) and (c) represent the gas and stellar instrument resolution (30 km/s and 70 km/s in (b)), and fitted kinematic measurement limit (23 km/s and 59 km/s in (c)). This figure shows that the gas and stellar estimates of V_{rot} and σ agree almost nowhere, while they agree moderately well for $S_{0.5} > 100$ km/s (but not at lower values).

be contaminated in their flux by either foreground stars or nearby bright galaxies in clusters. In the gas scaling relations, most outliers are found in the high mass ($\log M_* > 10$) and high $S_{0.5}$ measurement ($\geq 10^{2.5}$ km/s) area. These are ETG with relatively larger errors in their gas kinematic measurements. These outliers disappear when we apply a quality cut tighter than $\Delta S_{0.5}/S_{0.5} \leq 0.05$.

Once we find the $M_{*,\rm lim}$ value for each of the gas and stellar versions of the scaling relation, we convert them to $S_{0.5,\rm lim}$ using the linear fit. The fitting results from Figure 3 are shown in Table 2.

For the stellar version of the scaling relation, the bend occurs at $(M_{*,\rm lim,stellar},\ S_{0.5,\rm lim,stellar}) = (10^{9.6}, 59)$, and for the gas version, $(M_{*,\rm lim,gas},\ S_{0.5,\rm lim,gas}) = (10^{8.9}, 23)$. The fact that the bend in the scaling relations occurs at different stellar mass values suggests the nature of the bend in our scaling relation is more likely to be a measurement limit than a physical phenomenon. An interesting observation is that both $S_{0.5,\rm lim}$ values are close to, but somewhat below the instrumental dispersion resolution, they are below the instrument resolutions ($\sigma_{\rm res,gas} = 30$ km/s, $\sigma_{\rm res,stellar} = 70$ km/s). This suggests that not being able to measure the dispersion much below the instrumental dispersion (at least at the typical S/N per spaxel of the SAMI spectra) may be resulting in the apparent lower limit to $S_{0.5}$ and hence the apparent bend in the $\log M_* - \log S_{0.5}$ scaling relation.

3.3 Gas & stellar $S_{0.5}$ disagreement

To test whether the $S_{0.5}$ parameters from the stellar and gas kinematics trace the same gravitational potentials, we compare the rotation velocities, velocity dispersions and $S_{0.5}$ measurements of stellar and gas components on a per-galaxy basis with SAMI samples C, D and E (as described in Table 1). Galaxies in each sample are selected to have both gas and stellar kinematic errors less than 5%. Figure 4a, using sample C, shows that stars in general rotate more slowly than the gas. This is due to asymmetric drift, where the rotation velocity of the stars is lower than that of the gas because stars have additional pressure support against gravity from a higher dispersion (Binney & Tremaine 2008). The mean ratio between the stellar and gas rotation velocities is $\langle V_{rot,stellar}/V_{rot,gas}\rangle \sim 0.77 \pm 0.29$ which is consistent with the result obtained by Cortese et al. (2014) (~ 0.75).

Using sample D where both gas and stellar σ measurements have less than 5% error, the offset between the SAMI gas and stellar FJ relations observed in Cortese et al. (2014) is reflected in our FJ relation. The mean ratio between gas and stellar dispersions is $\langle \sigma_{stellar}/\sigma_{gas}\rangle \sim 1.58 \pm 0.59$, as shown in Figure 4b, consistent with the observation in Cortese et al. (2014)($\sim$ 1.55). There are galaxies with $\log \sigma_{gas} > 2.5$ that lie significantly above the one-to-one line. These are almost entirely elliptical and S0 galaxies. These galaxies have low gas abundance, hence relatively larger uncertainties in σ_{gas}, as shown in Figure 4b.

In Cortese et al. (2014), the gas and stellar $S_{0.5}$ parameters are found to have a mean logarithmic difference (gas − stellar) of -0.02 dex. In our sample D, the logarithmic difference is -0.05 dex. In Figure 4c, while the one-to-one line (black solid) indeed goes through our $S_{0.5,gas} - S_{0.5,stellar}$ distribution, the best-fit (red-dashed) line has a slope of 1.49 ± 0.02, which suggests a disagreement between $S_{0.5,gas}$ and $S_{0.5,stellar}$. The scatter in the $S_{0.5,gas} - S_{0.5,stellar}$ correlation increases for galaxies with $\log S_{0.5,gas} > 2.25$. Similarly to Figure 4b, this increase in scatter can be explained by elliptical and S0 galaxies having larger uncertainties in their σ_{gas} measurements. However, in the *hyper-fit* routine, measurements with large uncertainty are weighed less to reduce their impact on the fit parameters; with a tighter uncertainty cut using galaxies with only 2% error, the slope (1.34 ± 0.04) remained significantly above unity. We also modified the sample to only include galaxies with both gas and stellar measurements above the fitted kinematic measurement limit, and the slope remained at 1.49 ± 0.02. The disagreement between stellar and gas $S_{0.5}$ parameters requires an investigation on a per-galaxy basis, especially for lower mass ($\log M_* < 9.5$) galaxies where $S_{0.5,stellar} > S_{0.5,gas}$. This is beyond the scope of this work, and will be studied in more detail in future.

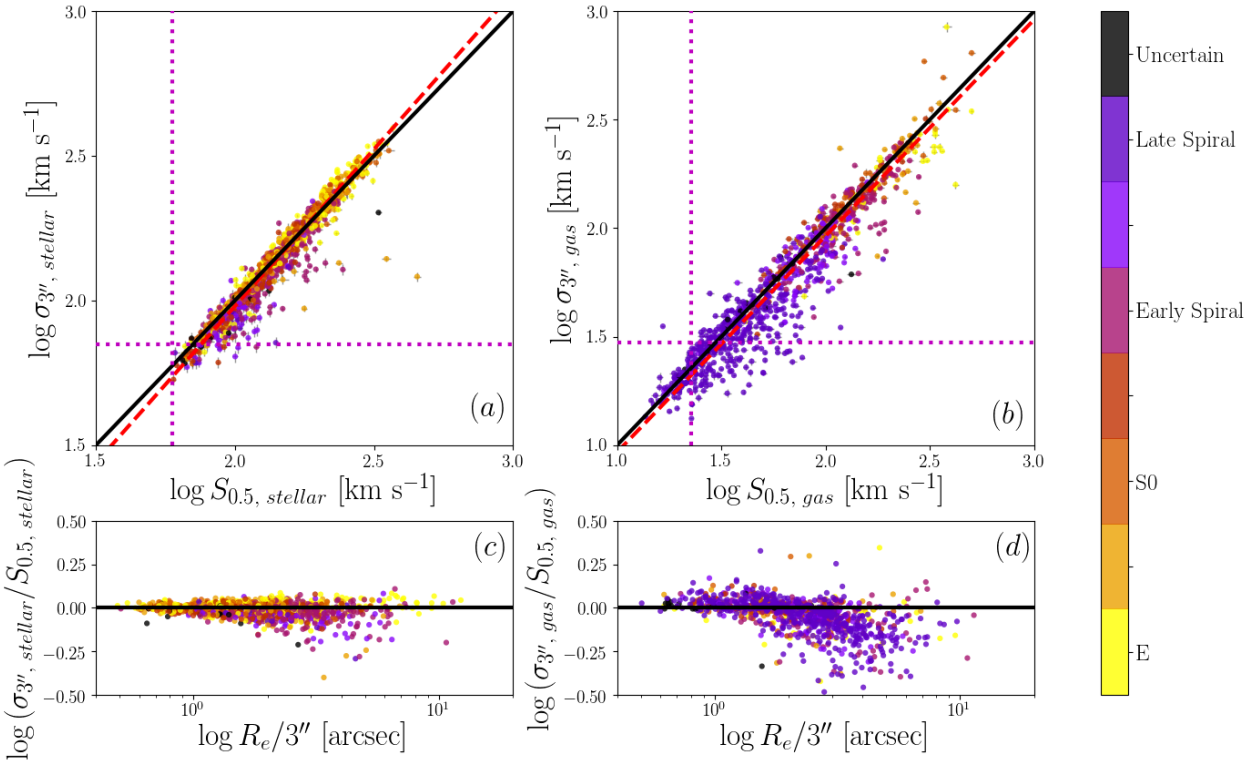

Figure 5. Direct comparison using sample F, between the $S_{0.5}$ parameter and the 3-arcsecond-diameter aperture velocity dispersion from gas and stellar kinematics, and their difference against apparent galaxy size. Black solid lines in panel (a) and (b) are one-to-one relations. Red dashed lines are lines of best fit. Horizontal and vertical magenta lines represent the instrument dispersion (70 km/s in (a), 30 km/s in (b)), and fitted kinematic measurement limit (59 km/s in (a) and 23 km/s in (b)) for the stellar and gas kinematics. Points are colour coded by morphologies.

3.4 IFS and aperture kinematics correlation

While IFS data provides spatial information on galaxy kinematics, one can also simulate a single fibre observation from the data cubes. We constructed aperture spectra from SAMI data cubes within a 3-arcsecond-diameter (SDSS-like) aperture. Applying a 5% error quality cut to the aperture velocity dispersions, we obtained $\sigma_{3'',gas}$ for 980 galaxies, and $\sigma_{3'',stellar}$ for 1250 galaxies; these form sample F (see Table 1). Figure 5 shows a comparison between $S_{0.5}$ parameter and $\sigma_{3''}$, and their logarithmic difference as a function of $R_e/3''$, the relative ratio of size and aperture diameter.

For stellar measurements, shown in Figure 5a, $S_{0.5,stellar}$ and $\sigma_{3'',stellar}$ form a remarkably tight relation with a scatter of 0.013 ± 0.001 dex. The fitted (red-dashed) line has a slope of 1.08 ± 0.01 which differs from unity due to late-type spiral galaxies whose $S_{0.5,stellar}$ measurements are larger than their aperture dispersion measurements. The outliers in Figure 5a correspond to those found in Figure 3a, which have flux contamination due to nearby bright objects. The difference between $\sigma_{3'',stellar}$ and $S_{0.5,stellar}$ shown in Figure 5c does not seem to trend with galaxy size as much as with morphology. For elliptical and S0 galaxies, aperture dispersions are similar to their $S_{0.5}$ measurements, whereas some spiral galaxies have larger $S_{0.5}$ measurements, which stems from inclination over-correction in the V_{rot} component of $S_{0.5}$.

For gas measurements, the $\log \sigma_{3'',gas} - \log S_{0.5,gas}$ comparison in Figure 5b shows a larger scatter (0.036 ± 0.001) than $\log \sigma_{3'',stellar} - \log S_{0.5,stellar}$. This is expected because the gas sample is dominated by LTGs, which have extended gas distributions that result in a strongly increasing rotation velocity with radius out to R_e (and beyond). Therefore the $S_{0.5,gas}$ measurements for late-type spiral galaxies will be larger than their $\sigma_{3''}$ measurements due to the larger V_{rot} component in the $S_{0.5}$ parameter. The $\sigma_{3'',gas} - S_{0.5,gas}$ distribution has a slope of 1.00 ± 0.01. The logarithmic difference between $\sigma_{3'',gas}$ and $S_{0.5,gas}$ in Figure 5d shows a negative trend over the angular sizes of galaxies. The scatter of the logarithmic difference also increases as a function of angular size. This correlation is a direct result of limiting the aperture dispersion within 3 arcsecond whereas $S_{0.5}$ is sampled as far as the field of view allows.

Even though the $S_{0.5}$ parameter and single aperture velocity dispersion $\sigma_{3''}$ for the gas and the stars cover different parts of galaxies, they remain in broad agreement. This agreement is encouraging because while the $\log M_* - \log S_{0.5}$ relation applies to galaxies of all morphologies, obtaining the $S_{0.5}$ parameter requires IFS data, hence is observationally expensive, whereas velocity dispersions from single-fibre surveys are observationally cheap. The residual plots in Figure 5c indicates that $\sigma_{3''}$ is a fairly unbiased predictor of $S_{0.5}$ out to about $R_e = 3''$ (rather than as one might have

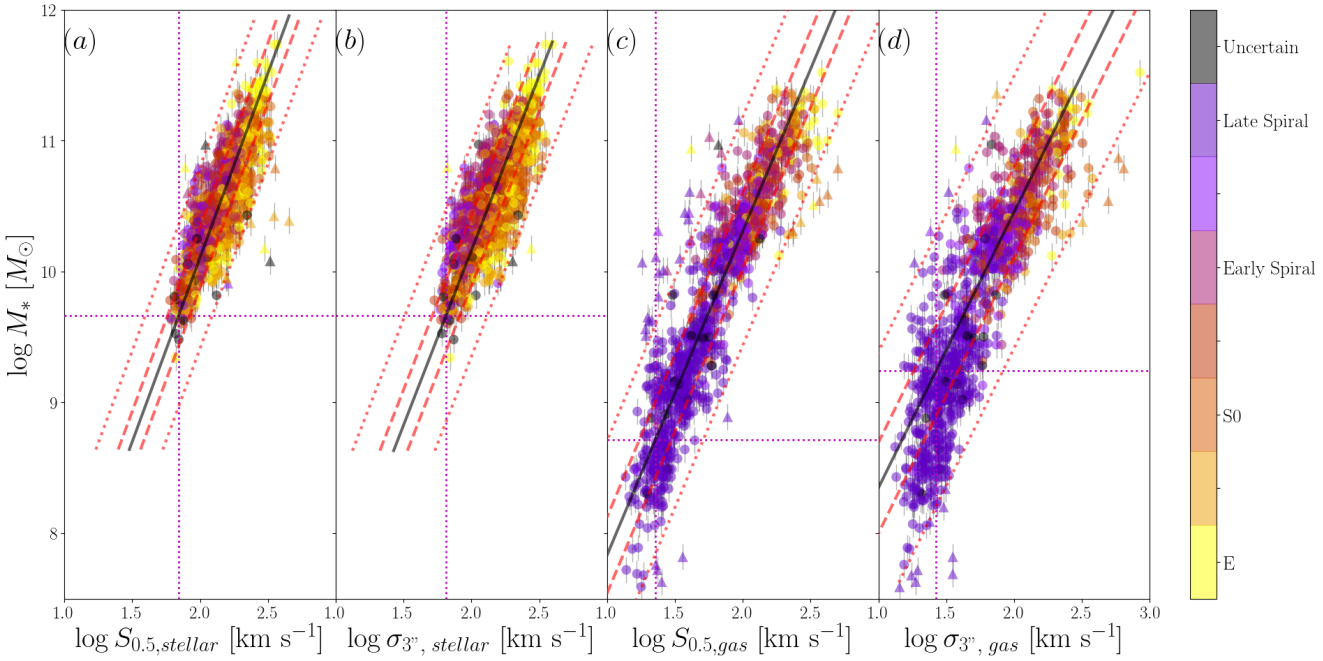

Figure 6. Scaling relations constructed from $S_{0.5}$ kinematic parameters and aperture velocity dispersions using sample F. Panel (a), (b), (c) and (d) show scaling relation constructed between stellar mass, and $S_{0.5,stellar}$, $\sigma_{3\prime\prime,stellar}$, $S_{0.5,gas}$, $\sigma_{3\prime\prime,gas}$ measurements. Black solid lines in each panel are lines of best fit. Red dashed and dotted lines define distances 1 RMS and 3 RMS away from the line of best fit. Triangular points are measurements >3 RMS away from the line of best fit, and are excluded from the fit. Horizontal and vertical magenta dotted lines are the fitted kinematic measurement limits. Fitting information are given in Table 2. For both gas and stellar components, $S_{0.5}$ for gas and stellar components consistently produces scaling relations with less scatter than aperture velocity dispersion.

expected $R_e = 3\prime\prime/2$), and the scatter only grows relatively gradually beyond $R_e = 3\prime\prime$, and more slowly for the stellar measurements than for the gas measurements.

3.5 Comparing IFS and aperture scaling relations

As both aperture σ and $S_{0.5}$ are used in kinematic scaling relations, we compare variants of the FJ and TF relations using $S_{0.5}$, and $\sigma_{3\prime\prime}$ in Figure 6. For both stellar and gas versions, using the $S_{0.5}$ parameter consistently provides tighter relations with less scatter than using $\sigma_{3\prime\prime}$. This confirms that $S_{0.5}$ serves as a better mass proxy than single aperture velocity dispersion, and suggests the promising possibility of reducing the scatter using $S_{0.5}$ in the construction of other scaling relations such as the FP relation (e.g. Graham et al. 2017). On the other hand, for many purposes the slight increase in scatter in the scaling relation that results from using the aperture dispersion rather than $S_{0.5}$ (~ 0.02 dex, from 20% to 25% for stars and from 29% to 36% for gas) may be an acceptable trade-off for the lower observational cost of single-fibre surveys relative to IFS surveys.

We notice that in Figure 6, choosing $S_{0.5}$ over $\sigma_{3\prime\prime}$ yields more outliers (triangular points, excluded from the fit) that are $>$ 3 RMS (red dotted line) away from the line of best fit (black solid line). This is due to factors such as inclination errors and individual spaxel quality. IFS sampling radius affects the quality of the $S_{0.5}$ parameter more than single aperture velocity dispersion measurements. In SAMI $\sigma_{3\prime\prime}$ measurements, spectra from each spaxel are co-added to form the aperture spectrum, which increases the signal-to-noise ratio, and returns more reliable kinematic measurements.

	Gas All	Gas ETG	Gas LTG
Optimal K	0.4	0.4	0.2
$\mathrm{MAD_{orth}}$	0.076	0.079	0.057
	Stellar All	**Stellar ETG**	**Stellar LTG**
Optimal K	0.7	0.3	0.2
$\mathrm{MAD_{orth}}$	0.045	0.044	0.047

Table 3. Values of K that return the minimum scatter for gas and stellar scaling relations for each morphological sample.

3.6 Varying K

The original S_K parameter introduced by Weiner et al. (2006) combines the galaxy rotation velocity and velocity dispersion in quadrature, and weighs the rotation velocity with K. This factor is commonly taken to be $K = 0.5$, which is correct only for virialised systems with spherical symmetry and isotropic velocity dispersion (Kassin et al. 2007). We test the effect of changing the value of K in the construction of the S_K parameter by exploring the influence K has on the scatter of the scaling relations. In this section we use sample G where each galaxy has V_{rot} and σ for gas and stellar kine-

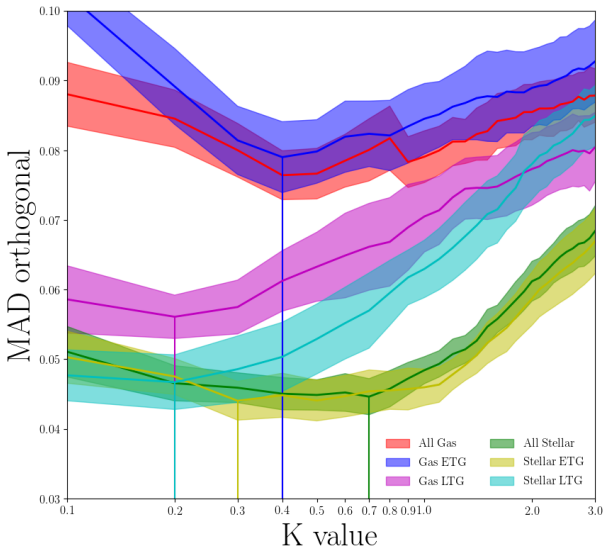

Figure 7. Effect of K value choice on the scatter of SAMI gas and stellar scaling relations, with the shaded region representing the 1σ uncertainty. Gas and stellar samples are further divided into ETGs and LTGs to compare the effect of morphology on the optimal K values. Where $S_{K,gas}$ is used the full, ETG and LTG samples are colour-coded red, blue and purple respectively. Where $S_{K,stellar}$ is used the full, ETG and LTG samples are colour-coded green, yellow and cyan respectively.

matic with less than 10% error. We chose 10% error on V_{rot} and σ to ensure there remains a statistically large number of galaxies to work with across all the K values.

We tested K values ranging from 0 to 3 in the $\log M_* - \log S_K$ scaling relation, and measured the orthogonal median absolute deviation from the scaling relation for each K value. We performed this test for both the gas and stellar versions of the scaling relation. We also divided the gas and stellar measurements into early-type (elliptical and S0) galaxies, and late-type (spiral and irregular) galaxies. We then measured the scatter in the scaling relation at every K value for each morphological group.

Figure 7 shows the effect of varying K in the $\log M_* - \log S_K$ scaling relation for gas and stellar measurements, and early-type and late-type galaxies. As seen from the figure, for the gas version of the scaling relation, the minima of the scaling relations are relatively sharp, whereas for the stellar version the minima are broader. The values of K that return the minimum scatter for each version of the scaling relation are listed in Table 3. However, given the uncertainties in the scatter measurements, shown as shaded regions in Figure 7, $K = 0.5$ returns a scatter consistent with the minimum scatter when either only ETGs or all galaxies are considered. This consistency justifies the common usage of $K = 0.5$ in the literature and the consistencies of analyses when K is varied (e.g. Covington et al. 2010; Cortese et al. 2014; Aquino-Ortíz et al. 2018). For LTGs, in both gas and stellar measurements, $K = 0.2$ returns the minimum scatter. The factors that lead to these optimal values are discussed further in the following section.

4 DISCUSSION

4.1 SAMI scaling relations

Using integral field spectroscopy from the SAMI survey for a parent sample of 2720 galaxies, we examine the $\log M_* - \log S_{0.5}$ scaling relation studied in Cortese et al. (2014). We confirm that the $S_{0.5}$ kinematic parameter, measured from either the stars or the gas, brings galaxies of all morphologies onto the same scaling relation with stellar mass. The slope of the scaling relation obtained here, whether for the stars (0.38 ± 0.01), or for the gas (0.44 ± 0.01), is steeper than those obtained from Cortese et al. (2014)(0.34 ± 0.01); this difference is likely due to differences in sample properties and fitting methods.

Cortese et al. (2014) observed a change in slope across a mass range of $8.5 \lesssim \log M_* \lesssim 11.5$, and suspected the slope change could be due to lack of HI measurements to include the effect of gas mass; we were also unable to test this as we did not have HI data available. However, we noted that the slope changes at different galaxy masses for the kinematic measurements from stars and gas, which suggested a kinematic measurement limit rather than a physical change in the scaling relation itself. We therefore fitted a linear scaling relation with a cutoff at some lower limit in $S_{0.5}$, and found that the fitted limits in the stellar and gas versions of the relation were each about 80% of the corresponding instrumental resolution limits. We therefore concluded that for masses higher than those corresponding to our kinematic measurement limit ($\log M_* > 9.6$ in the stellar case and $\log M_* > 8.9$ in the gas case) the $\log M_* - \log S_{0.5}$ scaling relation is linear. This is not to say that the scaling relation does not become non-linear at some lower mass. Aquino-Ortíz et al. (2018) suggest galaxies with stellar mass below $\log M_* \sim 9.5$ have more dark matter content within the effective radius as the mass decreases, hence the dynamical mass (from $S_{0,5}$ estimation) to stellar mass ratio for low mass galaxies increases. This explanation indeed results in a change in slope in the $\log M_* - \log S_{0.5}$ scaling. Unfortunately, while we do have galaxies in our sample with stellar mass below $\sim 3 \times 10^9 M_\odot$, the range of low mass galaxies does not extend low enough ($\sim 10^7 - 10^8 M_\odot$) to test for a change in slope. Higher spectral resolution ($\sigma_{\rm res} \sim 10$ km/s) IFS observations (e.g. from Hector, Bryant et al. 2016) of low-mass galaxies are necessary to fully determine the the linearity of the stellar scaling relation throughout the $7 \lesssim \log M_*/M_\odot \lesssim 12$ mass range.

4.2 IFS and aperture kinematics

In Section 3.4 and 3.5 we compared measurements of the $S_{0.5}$ parameter, and the aperture velocity dispersion and found surprisingly good agreement between the two kinematic tracers. This agreement is interesting because while both $S_{0.5}$ and $\sigma_{3''}$ are measures of velocity dispersion, the sources of velocity dispersion are different. By definition, $\sigma_{3''}$ measures the second moment of the LOSVD integrated over a 3-arcsecond-diameter aperture, including the effect of rotation velocity. For $S_{0.5}$, the σ component is a luminosity-averaged quantity from LOSVD dispersions distributed over an aperture (here R_e). However, simply including V_{rot} in $S_{0.5}$ not only conveniently correlates $S_{0.5}$ to $\sigma_{3''}$ (as seen in Section 3.4), but also creates tighter scaling relations with

$S_{0.5}$ than $\sigma_{3''}$ when compared to M_* (as seen in Section 3.5). This fact shows that the extra information provided by IFS and the more complex calculation involved in deriving $S_{0.5}$ can provide a better understanding of this scaling relation (and others). On the other hand, IFS is observationally expensive while fibre surveys are observationally cheap. So for some purposes requiring very large samples (e.g. exploring the effect of environment on scaling relations for galaxies of different morphological types, or using scaling relations to derive distances and peculiar velocities), aperture dispersions may be a better choice.

4.3 The importance of K

The motivation for using $K = 0.5$ in the S_K parameter originates from the virial theorem prediction of circular velocity and velocity dispersion relation for an isothermal sphere, $V_{circ} \propto \sqrt{\alpha} \cdot \sigma$, where α is a constant that describes the density profile of the system. We find the scatter weakly depends on the value of K, with minimum scatter occurring between $K = 0.2$ and $K = 0.7$.

There are a number of possible factors that can theoretically influence the value of K:

(1) *Solutions to the Jeans equation.* The convention of $K = 0.5$ originates from the singular sphere case of the Jeans equation where the circular velocity is given by:

$$V_{circ}^2 = \frac{GM(r)}{r} = -\sigma^2 \frac{d\ln\rho}{d\ln r} \tag{9}$$

where ρ and r are the density and radius of the sphere. For isothermal spheres, $\rho \propto \sigma^2/r^2$, and at large radius, $d\ln\rho/d\ln r \sim -2$; therefore $V_{circ}^2 \sim 2\sigma^2$(Section 4.3.3b, Binney & Tremaine 2008). Given we measured the V_{rot} via the velocity width technique, $V_{rot}^2 \equiv V_{circ}^2 \sim 2\sigma^2$. This derivation requires the assumptions of the specific density profile and the radius at which the kinematic is measured. In addition, almost no real galaxies satisfy these assumptions. However, as we see in Section 3.6, $K = 0.5$ is still close to optimal.

(2) *Velocity distribution function.* The value of K depends on the velocity distribution function of a galaxy, and in particular on the bulge-to-disk ratio and the V/σ ratio for each of the bulge and disk components. In the case of pressure-supported systems with negligible rotation, the average stellar line-of-sight velocity dispersion $\overline{\sigma}_{LOS}$ is a weighted sum of directional components $\sigma_r, \sigma_\theta, \sigma_\phi$. Excluding observational artefacts, the combination of components is dictated by the anisotropy parameter (Binney & Tremaine 2008, Eq 4.61)

$$\beta \equiv 1 - \frac{\sigma_\theta^2 + \sigma_\phi^2}{2\sigma_r^2}. \tag{10}$$

Depending on whether the distribution function of stars is tangentially biased ($\beta < 0$), radially biased ($\beta > 0$) or isotropic ($\beta = 0$), the combination of $\sigma_r, \sigma_\theta, \sigma_\phi$ making up $\overline{\sigma}_{LOS}$ will be different. Thus the K value needs to be adjusted to correct for the unobserved components of $\overline{\sigma}_{LOS}$.

(3) *Observational artefacts.* Given our best K value is determined by comparing the scatter in the $\log M_* - \log S_{0.5}$ relation, the quality of kinematic parameter measurements and the scatter of the scaling relation are crucial. Covington et al. (2010) have shown with numerical simulations that instrument blurring effects such as spatial resolution and seeing, which contribute to the scatter in the TF relation, do not show significant effects on the measured $S_{0.5}$ values. Aquino-Ortíz et al. (2018) also performed a detailed kinematic analysis with spatially resolved rotation velocity measurements. They found that the $S_{0.5}$ parameter consistently reduced the scatter in scaling relations, taking into account the uncertainties in the V_{rot} measurement for dispersion-dominated systems. In Section 3.2, we see that the instrument resolution limit for typical S/N ratios, if not taken into consideration in the fitting routine, can result in a change the slope of the scaling relation, and increase the scatter. Thus the best K value is determined by a combination of intrinsic dynamical properties and observational artefacts. In order to use the $\log M_* - \log S_K$ scaling relation to predict physical attributes of observed systems, it is crucial to make sure the scatter in the scaling relation is not dominated by systematic error.

5 CONCLUSIONS

In this paper we present the $\log M_* - \log S_{0.5}$ scaling relation constructed from the SAMI Galaxy Survey. The $S_{0.5}$ parameter is useful in bringing galaxies of all morphologies onto the same relation. Without sample pruning other than S/N quality cuts, the scatter in the $\log M_* - \log S_{0.5}$ relation is significantly less than the TF and FJ relations constructed from the same sample. Interestingly, only performing relative error cut on $S_{0.5}$ without any spaxel-level quality cut still provides a tight scaling relation. Through combined linear and cut off model fitting, we found that the change in slope occurs ∼10 km/s below our instrument dispersion resolution limits for gas and stellar kinematics. Although this does not exclude the possibility of a linear relation at the lower-mass ($\log M_*/M_\odot < 9$) end of the scaling relations, for our sample the change in slope appears to be due to kinematic measurement limits.

Comparing $S_{0.5}$ to single-aperture velocity dispersion $\sigma_{3''}$ shows excellent agreement between the two parameters. The gas $\sigma_{3'',gas} - S_{0.5,gas}$ residuals negatively trend with galaxy angular size, while stellar $\sigma_{3'',gas} - S_{0.5,gas}$ residuals show no correlation with galaxy angular size. In constructing scaling relations, $S_{0.5}$ consistently produced less scatter than $\sigma_{3''}$ when compared to stellar mass.

In order to test the importance of choosing an optimal value of K in the construction of the S_k parameter, we measured the scatter of the scaling relations at different values of K. By investigating the correlation between the scatter of the scaling relation and the value of K in the S_K parameter, we found that $K = 0.5$ for gas or stellar measurement is consistent with values that gave the least scatter for a pure ETGs sample, or a mixture of ETGs and LTGs. Only for pure LTGs sample, $K = 0.2$ gave significantly less scatter.

These findings are consistent with previous studies by Cortese et al. (2014) using early release of SAMI data, as well as Aquino-Ortíz et al. (2018) using CALIFA data.

The $S_{0.5}$ kinematic parameter has proven to be a valuable way of constructing a robust and inclusive galaxy scaling relation, and with the tight $S_{0.5} - \sigma_{3''}$ correlation, $S_{0.5}$ also paves the way for a scaling relation for galaxies of all morphologies with large-scale single fibre galaxy surveys.

ACKNOWLEDGEMENTS

The SAMI Galaxy Survey is based on observations made at the Anglo-Australian Telescope. The Sydney-AAO Multi-object Integral field spectrograph (SAMI) was developed jointly by the University of Sydney and the Australian Astronomical Observatory. The SAMI input catalogue is based on data taken from the Sloan Digital Sky Survey, the GAMA Survey and the VST ATLAS Survey. The SAMI Galaxy Survey is supported by the Australian Research Council Centre of Excellence for All Sky Astrophysics in 3 Dimensions (ASTRO 3D), through project number CE170100013, the Australian Research Council Centre of Excellence for All-sky Astrophysics (CAASTRO), through project number CE110001020, and other participating institutions. The SAMI Galaxy Survey website is http://sami-survey.org/.

DB is supported by an Australia Government Research Training Program Scholarship and ASTRO 3D. JBH is supported by an ARC Laureate Fellowship that funds JvdS and an ARC Federation Fellowship that funded the SAMI prototype. JJB acknowledges support of an Australian Research Council Future Fellowship (FT180100231). JvdS is funded under Bland-Hawthorn's ARC Laureate Fellowship (FL140100278). NS acknowledges support of a University of Sydney Postdoctoral Research Fellowship. SMS acknowledges parts of this research were conducted by ASTRO 3D, through project number CE170100013. BC acknowledges parts of this research were conducted by ASTRO 3D, through project number CE170100013. SB acknowledges the funding support from the Australian Research Council through a Future Fellowship (FT140101166). SMC acknowledges the support of an Australian Research Council Future Fellowship (FT100100457). BG is the recipient of an Australian Research Council Future Fellowship (FT140101202). M.S.O. acknowledges the funding support from the Australian Research Council through a Future Fellowship (FT140100255).Support for AMM is provided by NASA through Hubble Fellowship grant HST-HF2-51377 awarded by the Space Telescope Science Institute, which is operated by the Association of Universities for Research in Astronomy, Inc., for NASA, under contract NAS5-26555.

REFERENCES

Ahn C. P., Alexandroff R., Allende Prieto C., et al. 2012, ApJS, 203, 21
Allen J. T., et al., 2014, SAMI: Sydney-AAO Multi-object Integral field spectrograph pipeline, Astrophysics Source Code Library (ascl:1407.006)
Allen J. T., Croom S. M., Konstantopoulos I. S., et al 2015, MNRAS, 446, 1567
Aquino-Ortíz E., Valenzuela O., Sánchez S. F., Hernández-Toledo H., et al 2018, MNRAS, tmp, 1451
Binney J., Tremaine S., 2008, Galactic Dynamics. Princeton University Press
Bland-Hawthorn J., Bryant J., Robertson G., et al 2011, Optics Express, 19, 2649
Bryant J. J., Bland-Hawthorn J., Fogarty L. M. R., Lawrence J. S., Croom S. M., 2014, MNRAS, 438, 869
Bryant J. J., Owers M. S., Robotham A. S. G., Croom S. M., 2015, MNRAS, 447, 2857
Bryant J. J., et al., 2016, in Ground-based and Airborne Instrumentation for Astronomy VI. p. 99081F (arXiv:1608.03921), doi:10.1117/12.2230740
Cappellari M., Emsellem E., 2004, Publications of the Astronomical Society of the Pacific, 116, 138
Catinella B., Haynes M. P., Giovanelli R., 2005, AJ, 130, 1037
Catinella B., Giovanelli R., Haynes M. P., 2012, ApJ, 640, 751
Cortese L., Fogarty L. M. R., Ho I.-T., Bekki K., 2014, ApJ, 795, L37
Cortese L., et al., 2016, MNRAS, 463, 170
Covington M. D., Kassin S. A., Dutton A. A., et al 2010, The Astrophysical Journal, 170, 279
Croom S. M., Lawrence J. S., Bland-Hawthorn J., Bryant J. J., 2012, MNRAS, 421, 872
Desmond H., Wechsler R. H., 2017, MNRAS, 465, 820
Djorgovski S., Davis M., 1987, ApJ, 313, 59
Dressler A., Lynden-Bell D., Burstein D., Davis R. L., Faber S. M., Terlevich R., Wegner G., 1987, ApJ, 313, 42
Emsellem E., Monnet G., Bacon R., 1994, Astronomy and Astrophysics, 285, 723
Faber S. M., Jackson R. E., 1976, ApJ, 204, 668
Foreman-Mackey D., Hogg D. W., Lang D., Goodman J., 2013, PASP, 125, 306
Graham A. W., Janz J., Penny S. J., Chilingarian Igor V.and Ciambur B. C., 2017, Apj, 840, 68
Ho I.-T., Kewley L. J., Dopita M. A., 2014, MNRAS, 444, 3894
Iodice E., Arnaboldi M., Bournaud F., Combes F., 2003, ApJ, 585, 730
Kassin S. A., Weiner B., Faber S. M., et al 2007, ApJ, 660, L35
Kassin S. A., Weiner B., Faber S. M., et al 2012, ApJ, 758, 106
Kelvin L. S., Driver S. P., Robotham A., et al 2014, MNRAS, 439, 1245
Kormendy J., 1977, ApJ, 218, 333
Lagos C. d. P., Theuns T., Stevens A. R. H., Cortese L., Padilla N. D., et al 2017, MNRAS, 464, 3850
McGaugh S. S., Schombert J. M., Bothun G. D., de Blok W. J. G., 2000, ApJ, 533, L99
Neistein E., Maoz D., Rix H.-W., Tonry J. L., 1999, AJ, 177, 2666
Obreschkow D., Glazebrook K., 2014, ApJ, 784, 26
Ouellette N. N., Courteau S., Holtzman J. A., Dutton A. A., et al 2017, ApJ, 843, 74
Robotham A. S. G., Obreschkow D., 2015, Publications of the Astronomical Society of Australia, 32
Sánchez S. F., Kennicutt R. C., Gil de Paz A., van de Ven G., Vilchez J. M., et al 2012, A&A, 538, 8
Scott N., van de Sande J., Croom S. M., Groves B., Owers M. S., et al 2018, MNRAS, tmp, 2240S
Shanks T., et al., 2015, MNRAS, 451, 4238
Sharp R., Saunders W., Smith G., 2006, Ground-based and Airborne Instrumentation for Astronomy. SPIE, Bellingham, 6269
Sharp R., et al., 2015, MNRAS, 446, 1551
Simons R. C., Kassin S. A., Weiner B. J., Heckman T. M., Lee J. C., Lotz J. M., Peth M., Tchernyshyov K., 2015, MNRAS, 452, 986
Straatman C. M. S., et al., 2017, ApJ, 839, 57
Tonini C., Jones D. H., Mould J., Webster R. L., 2014, MNRAS, 438, 3332
Tully R., Fisher J., 1977, A & A, 54, 661
Weiner B. J., Willmer C. N. A., Faber S. M., 2006, ApJ, 653, 1027
Williams M. J., Bureau M., Cappellari M., 2010, MNRAS, 409, 1330
van de Sande J., Bland-Hawthorn J., Fogarty L. M. R., Cortese L., D'Eugenio F., et al 2017, ApJ, 104, 35

This paper has been typeset from a TEX/LATEX file prepared by the author.